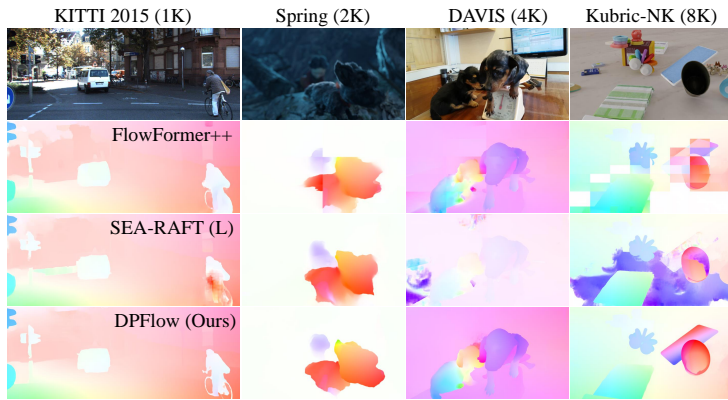
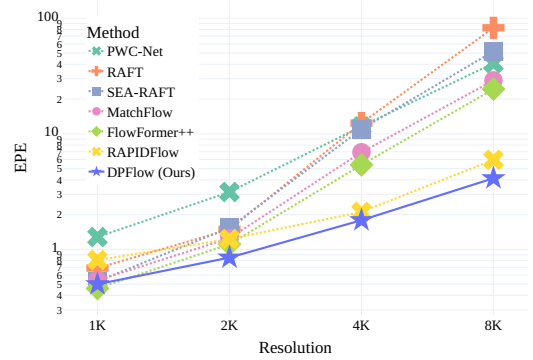


DPFlow: Adaptive Optical Flow Estimation with a Dual-Pyramid Framework

Henrique Morimitsu¹ Xiaobin Zhu¹ (✉) Roberto M. Cesar-Jr.² Xiangyang Ji³ Xu-Cheng Yin¹
¹University of Science and Technology Beijing ²University of São Paulo ³Tsinghua University
 {hmori, zhuxiaobin, xuchengyin}@ustb.edu.cn rmcasar@usp.br xyji@tsinghua.edu.cn



(a) Qualitative results at 1K, 2K, 4K, and 8K resolutions.



(b) Results on the proposed Kubric-NK evaluation.

Figure 1. (a) Optical flow results on multiple resolution images from the KITTI 2015 [36], Spring [35], DAVIS [40] and our proposed Kubric-NK datasets. Methods like FlowFormer++ [48] adopt tiling to handle high-resolution inputs, which causes square-shaped artifacts and loss of global context. Static approaches, such as SEA-RAFT [60], do not generalize well to large changes in resolution either. Our proposed DPFlow employs a flexible dual-pyramid design to adapt to larger inputs. (b) Our proposed Kubric-NK evaluation can quantify the generalization capabilities to resolutions up to 8K. At 8K, DPFlow outperforms RAPIDFlow [38] by 30% and FlowFormer++ by 83%.

Abstract

Optical flow estimation is essential for video processing tasks, such as restoration and action recognition. The quality of videos is constantly increasing, with current standards reaching 8K resolution. However, optical flow methods are usually designed for low resolution and do not generalize to large inputs due to their rigid architectures. They adopt downscaling or input tiling to reduce the input size, causing a loss of details and global information. There is also a lack of optical flow benchmarks to judge the actual performance of existing methods on high-resolution samples. Previous works only conducted qualitative high-resolution evaluations on hand-picked samples. This paper fills this gap in optical flow estimation in two ways. We propose DPFlow, an adaptive optical flow architecture capable of generalizing up to 8K resolution inputs while trained with only low-resolution samples. We also introduce Kubric-NK, a new benchmark for evaluating optical flow methods with input resolutions ranging from 1K to 8K. Our high-resolution evaluation pushes the boundaries

of existing methods and reveals new insights about their generalization capabilities. Extensive experimental results show that DPFlow achieves state-of-the-art results on the MPI-Sintel, KITTI 2015, Spring, and other high-resolution benchmarks. The code and dataset are available at <https://github.com/hmorimitsu/ptlflow/tree/main/ptlflow/models/dpflow>.

1. Introduction

Optical flow provides per-pixel video motion information, being essential for several video processing tasks, such as restoration [27], navigation [6], compression [55], and action recognition [46]. Due to the advance of technology, the quality and size of videos have been quickly increasing, with current video standards reaching 8K (7680 × 4320) resolutions. Nonetheless, most optical flow approaches are designed for only up to 1K resolution inputs and cannot generalize well to larger inputs (Fig. 1). Many methods [23, 63, 67] rely on global matching, but their quadratic computational costs limit them. Transformer-based [58] ap-

proaches [10, 48, 61] also struggle to adapt to changes in input size [15]. They usually adopt input tiling [15, 19] to overcome the input size limitations, but this strategy creates artifacts due to the loss of global context (Fig. 1a). Some other methods are not resource-restricted and can theoretically process inputs of larger sizes [56, 60, 62]. Nonetheless, they show significant estimation degradation with high-resolution inputs. This problem can be mitigated with high-resolution training [62]. However, this strategy is impractical for very large inputs.

Some existing methods have been shown to work with inputs of up to 4K resolution [62, 68]. However, they are only qualitatively evaluated on a few hand-picked samples, which does not offer enough evidence of their real generalization capabilities to changes in input size. Existing optical flow benchmarks only offer up to 2K densely annotated inputs [25, 35, 49]. TAP-Vid [8] has some 4K resolution samples, but they only provide annotations for a small set of sparse points per image. Therefore, there is a lack of quantitative benchmarks to evaluate the performance of optical flow methods on high-resolution inputs.

This paper fills these gaps in high-resolution optical flow estimation in two ways. First, we propose DPFlow, an optical flow architecture that uses a dual-pyramid bidirectional recurrent encoder to adapt to inputs of multiple sizes. Our method can be trained only with low-resolution samples and generalize well to 8K resolution inputs. DPFlow achieves state-of-the-art results on multiple public benchmarks. We achieve the best zero-shot and fine-tuning evaluation results on the higher-resolution Spring benchmark [35], outperforming SEA-RAFT [60] and RPKNet [39] by 6.5% and 10.8%, respectively. DPFlow also performs well on standard-resolution datasets, achieving the best overall ranking in the MPI-Sintel [5] and the KITTI 2015 [36] benchmarks.

Second, we created the Kubric-NK dataset, featuring 2400 densely annotated samples at four resolutions ranging from 1K to 8K. To the best of our knowledge, this is the first dataset to provide a platform for systematically evaluating the performance of optical flow methods with up to extremely large inputs. We use Kubric-NK to evaluate multiple existing optical flow methods and reveal new findings about how high-resolution inputs affect the predictions. In particular, we show that DPFlow has strong generalization capabilities, outperforming the next best method by more than 30% at 8K resolution (Fig. 1b).

In summary, our contributions are as follows:

1. We introduce DPFlow, an adaptive optical flow method that only uses standard-resolution samples for training but generalizes well to a wide range of input sizes.
2. We propose a recurrent bidirectional dual-pyramid encoder that combines variable image- and feature-pyramids to extract multi-scale features from inputs of

different sizes.

3. We create Kubric-NK, a dataset containing multi-resolution samples to push the boundaries of existing optical flow methods by evaluating them with inputs up to 8K resolution.
4. We demonstrate in extensive experiments that our DPFlow model achieves state-of-the-art optical flow prediction on multiple benchmarks, especially with higher-resolution inputs.

2. Related Works

2.1. Optical Flow Estimation

The use of multi-scale features for estimating optical flow in a coarse-to-fine manner has been a popular strategy adopted by classical approaches [3, 4] to handle large motions. This strategy has been adopted by multiple models to solve complex problems [11, 16, 41, 51, 52, 66]. Later, RAFT [56] introduced a paradigm shift by pairing single-scale features with iterative decoding to produce more accurate estimations. Since then, this architecture has become the foundation of most current approaches. Some methods adopted global matching strategies [63, 64, 67] to produce more reliable initial estimations at fast speeds. The use of the attention mechanism [58] has also been adopted by multiple models [10, 15, 23, 26, 32, 61, 64, 67] to encode more discriminative features. Some recent works have focused on exploring multi-frame strategies to handle more challenging scenes [9, 30, 47], significantly improving the estimation quality on longer sequences. However, these methods usually do not perform well when handling inputs whose sizes differ significantly from the training samples.

2.2. High-Resolution Approaches

Acknowledging the increasing demand for high-quality videos, a few optical flow methods have proposed ways to handle high-resolution inputs. Splitting the image with input tiling [15, 19] has been adopted by some top-performing methods [10, 48, 61] to get around their size limitations. Nonetheless, this strategy significantly increases latency and loses global contextual information. Flow1D [62] used 1D decomposition to avoid the quadratic cost of the 4D correlation stage to enable high-resolution processing. DIP [68] adopted local PatchMatch [2] with multi-scale features to replace the global matching stage and reduce computational costs. Recurrent networks have shown to be a flexible way to adapt to changes in input size [38, 50], although they have not been extensively evaluated for large optical flow prediction tasks. Based on these previous findings, DPFlow also adopts a recurrent architecture and further improves it with our dual-pyramid approach.

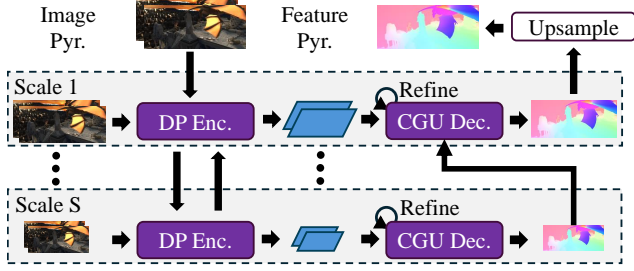


Figure 2. Overview of DPFlow architecture. The dual-pyramid encoder (DP Enc.) combines image and feature pyramids to extract multi-scale features, which the CGU Decoder iteratively refines to produce accurate optical flow predictions.

2.3. Optical Flow Datasets

Most optical flow datasets are composed of synthetic samples whose annotations can be automatically collected from the rendering engines. However, even synthetic optical flow datasets usually only provide low-resolution samples compared to current high-definition video standards. The samples from most commonly used optical flow datasets [5, 11, 34, 36, 59] are not larger than around 1000 (1K) pixels wide. Acknowledging the lack of higher-resolution data, some other datasets [22, 25, 35, 42, 49] provided samples with around double the resolution. While datasets with even larger inputs are available, they have a very limited amount of annotated data. For example, Middlebury-ST [44] provided only thirty-three samples at 3K resolution for stereo matching. TAP-Vid [8] provides some 4K resolution samples, but they only annotated a very sparse set of around twenty points per video. Therefore, there is a lack of data for evaluating the performance of optical flow models at high resolutions.

3. DPFlow

We adopt a recurrent encoder-decoder structure for optical flow prediction, similar to RAPIDFlow [38] and RPKNet [39]. However, we propose a novel recurrent dual-pyramid encoder to extract multi-scale features. This encoder builds on RPKNet and combines the advantages of image and feature pyramids in a flexible bidirectional recurrent structure. DPFlow employs a convolutional Cross-Gated Unit (CGU) to modulate the information flow to collect discriminative features at lower costs. Our decoder follows the structure of RAPIDFlow, but we adopt a GRU equipped with our CGU as the main refinement block. DPFlow’s structure is shown in Fig. 2.

3.1. Dual-Pyramid Encoder

Most methods use image or feature pyramids to extract multi-scale features from the inputs (Fig. 3). Image pyramids produce a single feature per level and provide a more

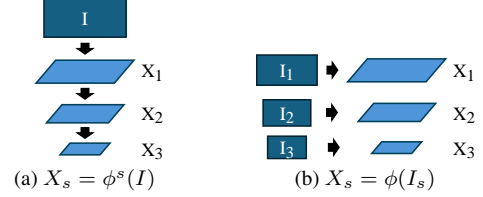


Figure 3. (a) Feature pyramid. (b) Image pyramid. ϕ represents a network block, I denotes images and X features.

direct path to the input information. On the other hand, feature pyramids transmit multi-scale information across levels, but the input information may be diluted in the deepest levels. Pyramids become even more challenging with a recurrent network that shares the same block across all levels, which may cause the gradients to vanish during training.

We propose to combine the properties of both pyramid approaches in a unified dual-pyramid encoder. This allows us to share multi-scale information across levels while using the image pyramid to retain access to input information at all levels. Our recurrent network adopts ConvGRU [1] to avoid training instability and better modulate the information flow across levels. Moreover, we adopt a bidirectional recurrent unit to allow shallower levels access to information from deeper levels. The pipeline of our recurrent dual-pyramid network is illustrated in Fig. 4 and described as:

$$\begin{aligned}
 X_0^f, H_0^f &= \phi^{\text{stem}}(I), \\
 H_s^f &= \text{ConvGRU}^f(H_{s-1}^f, X_{s-1}^f), \\
 X_s^f &= \text{CGU Block}^f(H_s^f), \\
 H_s^b &= \text{ConvGRU}^b(H_{s+1}^b, X_s^f), \\
 X_s^b &= \text{CGU Block}^b(H_s^b), \\
 X_s^i &= \phi^i(I_s), \\
 X_s &= \phi^{\text{out}}(\text{concat}(X_s^f, X_s^b, X_s^i)),
 \end{aligned} \tag{1}$$

where CGU Block is our Cross-Gated Unit block, I represents the original input image, and I_s is downsampled to the scale s . ϕ denotes a convolution block and the superscripts f, b, i denote forward, backward, and image, respectively. We initialize the state H^b as zero, and the output feature X_s is obtained by concatenating the intermediate forward, backward, and image pyramid features. The same process is applied to both images of the input pair.

3.2. Cross-Gated Unit (CGU)

Most models adopt self- and cross-attention [53, 58, 63] to extract more discriminative features for matching. However, attention mechanisms pose challenges, such as high computational costs and lack of generalization to different input sizes [15, 19]. CNNs avoid these problems using simpler local operations without requiring explicit posi-

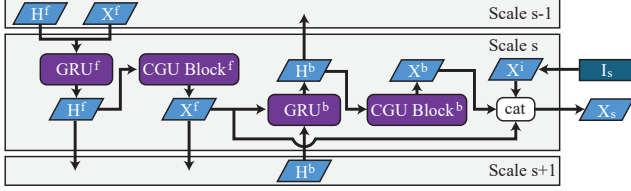


Figure 4. Illustration of the dual-pyramid encoder block.

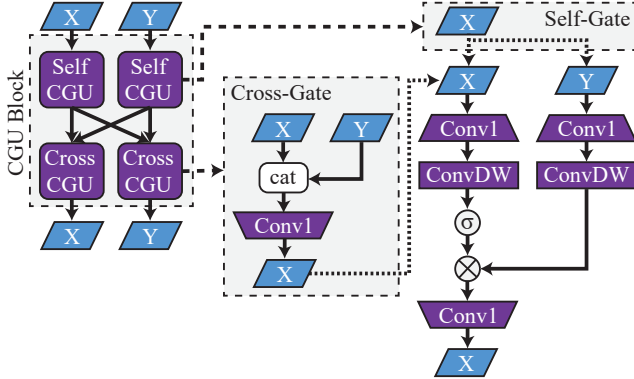


Figure 5. Illustration of the CGU block, composed of convolutional self- and cross-gates. Conv1 uses a 1×1 kernel, and ConvDW denotes depthwise convolution. We adopt GELU [14] as the non-linear gate σ and Layer Scale [57] to modulate the residual.

tional encoding [18]. Therefore, our DPFlow model adopts a pure convolution-based Cross-Gated Unit (CGU) as its main component. The CGU structure is illustrated in Fig. 5. Its design is inspired by the Gated-CNN block [7] with a cross-gate to leverage information from a pair of inputs. If only one input is provided, the CGU acts as a self-gate.

3.3. Loss Function

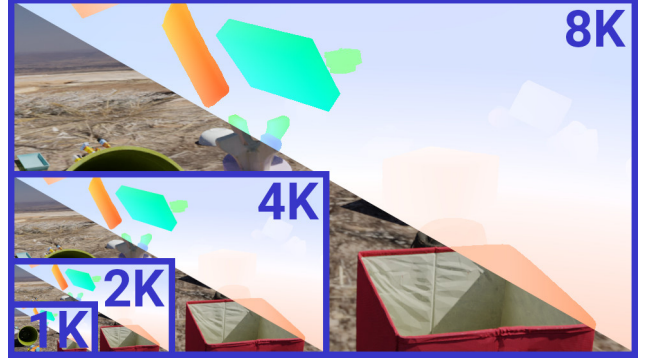
We train our model using the Mixture-of-Laplace loss [60] (\mathcal{L}_{MoL}) but adapted for multi-scale training. The MoL loss reduces the impact of points with ambiguous predictions that can otherwise dominate the loss term. We train our models using three scales and four iterations per scale. However, these settings can be freely changed during inference. Our loss function is hence defined as:

$$\mathcal{L}(F_{s,k}^{\text{pred}}, F) = \sum_{s=1}^3 \sum_{k=1}^4 \gamma^{4s-k} \mathcal{L}_{\text{MoL}}(F_{s,k}^{\text{pred}}, F), \quad (2)$$

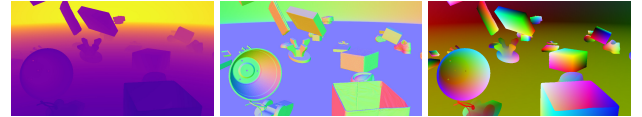
where γ is a scalar weight, F is the groundtruth flow and $F_{s,k}^{\text{pred}}$ is the prediction at scale s and refinement iteration k .

4. Kubric-NK Dataset

Optical flow methods require resolution generalization as flow vectors correlate with input spatial resolution. Nonetheless, current optical flow evaluation datasets do not



(a) Image pair and optical flow



(b) Depth

(c) Surface normals

(d) Object coordinates

Figure 6. The Kubric-NK dataset provides the same samples from 1K to 8K resolutions to test generalization to different input sizes.

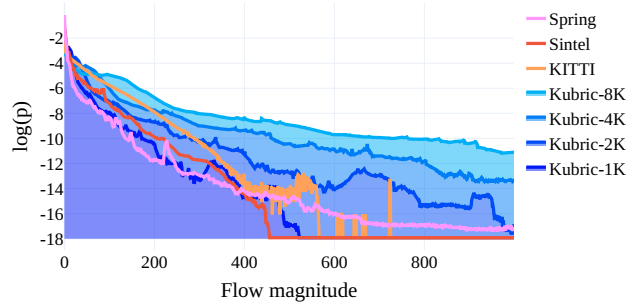


Figure 7. Comparison of flow magnitude distributions between Kubric-NK and other datasets.

provide a way to evaluate the robustness of optical flow methods to changes in resolution. Most papers [45, 62, 68] show generalization to high resolutions with only a few qualitative examples, which makes it hard to compare different methods. In this paper, we employ Kubric [12] to generate a multi-resolution synthetic optical flow dataset. We procedurally generate 30 sequences containing 600 unique densely annotated samples at four resolutions: 1K, 2K, 4K, and 8K. In addition to the optical flow, other dense annotations, such as depth, surface normals, and object coordinates, are also available. We define the input resolution nK as $(960n, 540n)$ and thus refer to our dataset as Kubric-NK. Figure 6 shows some samples from the proposed Kubric-NK dataset.

This dataset serves two main purposes: (1) to provide a common platform to quantitatively evaluate the performance of optical flow methods at high resolutions and (2) to analyze how input size changes affect different models by

providing the same scenes rendered at multiple resolutions. The histograms in Fig. 7 show that Kubric-NK optical flow samples at 1K resolution have a similar distribution to other popular datasets, such as MPI-Sintel [5]. At the same time, Kubric-NK’s provides significantly larger and more challenging samples at higher resolutions.

5. Experimental Results

5.1. Dataset and Implementation

We follow the traditional optical flow training pipeline of five stages. We do not use any additional high-resolution datasets for training. Stage 1 comprises 100k iterations on the FlyingChairs dataset [11]. Stage 2 adds 1M more iterations on the FlyingThings3D [34]. For stage 3, we use 120k iterations to finetune the model in a mixed dataset combining FlyingThings3D, KITTI 2015 [36], HD1K [25], and Sintel [5] samples. Stage 4a further finetunes the model in the KITTI 2015 dataset for 2k iterations. Stage 4b finetunes the model from stage 3 for 120k more iterations using the Spring [35] training samples. Our models are implemented in PyTorch and trained on two NVIDIA RTX3090 GPUs.

We evaluate the results on each dataset using their official metrics. MPI-Sintel, Middlebury-ST [44], and Kubric-NK adopt the End-Point-Error (EPE). Spring is evaluated with the 1-pixel (1px) metric, KITTI 2015 uses the Fl-All metric, while VIPER [42] uses their proposed WAUC metric. Additional details are provided in the Sup. Mat.

5.2. High-Resolution Evaluation

Previous works usually only provide qualitative evaluation for generalization to high-resolution inputs [62, 68]. Here, we provide quantitative metrics of current optical flow models on various existing high-resolution samples and our Kubric-NK dataset. Table 1 provides an overview of the datasets we use in our evaluation. The results are collected using open-source implementations of the models [37, 61]. DPFlow automatically chooses the number of pyramid levels N based on the diagonal input size: $N = \text{round}(\log_2(\max(1, \sqrt{W^2 + H^2}/\sqrt{960^2 + 540^2}))) + 3$ and adopts 4 refinement iterations per level.

5.2.1. Evaluation Checkpoint

Before testing each model, we must choose which training stage to use for the experiments. We evaluate the results of models trained with stages 2 and 3 on a subset of our chosen high-resolution datasets to check how each checkpoint behaves. Table 2 shows the average error obtained by a set of methods trained with each stage. Due to their large sizes, we use only 10% of Spring and VIPER samples for this evaluation. The selected methods list and their results are provided in the Sup. Mat. The results indicate that stage 3 training is the best choice, except for Middlebury-ST. Stage 3’s under-performance may be due to the low number of samples and

Table 1. Overview of the datasets used in our high-resolution experiments.

Dataset	Resolution	Train	Test
Spring [35]	2K (4K GT)	4963	3960
Middlebury-ST [44]	3K	23	-
VIPER [42]	2K	4954	-
Kubric-NK	1K, 2K, 4K, 8K	-	4×600

Table 2. Average results with different training stages. Results in bold indicate which stage we used for each dataset.

Dataset	Metric	Stage 2	Stage 3
Spring [35]	1px ↓	4.92	4.53
VIPER [42]	WAUC ↑	63.1	65.9
Middlebury-ST [44]	EPE ↓	24.3	32.9
Kubric-1K	EPE ↓	0.72	0.70

the stereo images. We use the results from Tab. 2 to choose the training checkpoint for each benchmark.

5.2.2. Spring Dataset

We conduct three tests with the Spring benchmark. The first test evaluates the model generalization using the train split of the dataset. Since Spring provides 4K annotations, our second test uses bicubic interpolation to double the resolution of the images and repeat the previous experiment (Spring 4K). For the last test, we used training stages 3 and 4b and submitted our results to the public zero-shot and finetuning benchmarks, respectively. Table 3 shows that DPFlow achieves the best results in all variants of the Spring benchmark. Regarding the public test results, DPFlow outperforms previous methods by over 6.5% in the zero-shot and fine-tuning settings. The advantage of our method becomes even more apparent in the 4K evaluation, where we outperform RAPIDFlow by 13%, thus demonstrating the advantage of our more robust dual-pyramid encoder. Compared to fixed-pyramid methods like SEA-RAFT [60], we achieve an even more notable improvement of 27%.

5.2.3. VIPER

The VIPER dataset provides FullHD resolution samples captured by a driving car in a video game. At this resolution, most methods produce reliable predictions. DPFlow performs on par with MatchFlow using the default pyramid. However, as shown in Tab. 8, better results could be achieved by tuning the pyramid levels.

5.2.4. Middlebury-ST

This dataset provides high-resolution real images for the task of stereo prediction. We use the samples with *imperfect* stereo alignments, making the task similar to optical flow

Table 3. Results on high-resolution datasets. In Spring, ft. indicates results obtained after fine-tuning the model with Spring samples, while 0-sh. is the zero-shot evaluation. † results are not available due to running out of memory. □ denotes methods that use input tiling [15, 19] and * methods with adaptive pyramids. The metrics of each dataset are explained in Sec. 5.1 and in the Sup. Mat.

Method	Venue	Spring (1px ↓)				VIPER	Mbury-ST	Kubric-NK			
		train		test-2K		WAUC ↑	EPE ↓	EPE ↓			
		2K	4K	ft.	0-sh.	2K	3K	1K	2K	4K	8K
PWC-Net [51]	CVPR'18	4.94	9.78	-	82.2	66.0	35.9	1.26	3.11	11.4	40.8
IRR [17]	CVPR'19	3.85	8.53	-	-	66.3	15.2	1.09	2.26	15.6	†
VCN [65]	NeurIPS'19	7.50	-	-	-	62.9	44.2	1.08	2.77	†	†
RAFT [56]	ECCV'20	3.85	10.7	-	6.79	71.1	35.2	0.68	1.46	12.3	82.7
GMA [23]	ICCV'21	3.75	†	-	7.07	71.7	†	0.66	1.30	†	†
DIP [68]	CVPR'22	3.64	9.53	-	-	71.3	16.7	0.68	1.57	5.12	†
GMFlow [63]	CVPR'22	6.71	†	-	10.35	56.7	†	0.88	1.38	†	†
FlowFormer [15]□	ECCV'22	3.78	9.53	-	6.51	72.7	19.0	0.52	1.04	5.60	24.4
SKFlow [54]	NeurIPS'22	3.79	†	-	-	71.9	†	0.62	1.07	†	†
FlowFormer++ [48]□	CVPR'23	3.76	9.71	-	-	72.5	17.5	0.46	1.11	5.39	24.4
MatchFlow [10]□	CVPR'23	3.97	9.32	-	-	73.0	16.7	0.54	1.25	6.93	29.0
CroCo-Flow [61]□	ICCV'23	3.51	†	4.56	-	76.1	†	0.45	1.06	†	†
MS-RAFT+ [20]	IJCV'23	<u>3.08</u>	†	-	5.72	-	†	0.55	1.27	†	†
GMFlow+ [64]	TPAMI'23	5.72	†	-	-	69.3	†	0.45	<u>0.97</u>	†	†
RPKNet [39]	AAAI'24	3.28	7.35	-	4.80	72.7	15.0	0.60	1.05	3.96	18.2
MemFlow [9]	CVPR'24	3.24	†	4.48	5.76	74.6	†	0.55	<u>0.97</u>	†	†
SEA-RAFT (M) [60]	ECCV'24	3.47	8.22	<u>3.68</u>	-	<u>75.5</u>	65.1	0.53	1.53	11.0	51.8
RAPIDFlow [38]*	ICRA'24	3.73	<u>6.91</u>	-	-	71.0	<u>6.41</u>	0.81	1.23	<u>2.11</u>	<u>5.96</u>
CCMR+ [21]	WACV'24	3.27	†	-	-	75.2	†	0.54	1.41	†	†
DPFlow*		3.06	6.03	3.44	4.28	72.9	5.03	0.50	0.85	1.77	4.11

estimation. With 3K resolution samples, the advantages of DPFlow are more evident. We obtain a 21% error reduction against RAPIDFlow and 66% against RPKNet.

5.2.5. Kubric-NK

We use Kubric-NK to analyze the behavior of optical flow models when the input size changes. The results in Tab. 3 and Fig. 1b reveal some new and important characteristics of optical flow methods.

Scaling behavior. The input size directly affects the flow magnitude, causing higher errors at larger resolutions. Methods based on single-resolution features, such as RAFT [56] variants, show exponential degradation when the resolution increases (e.g., SEA-RAFT's estimation error increases by two orders of magnitude from 1K to 8K). Using multi-scale features (RPKNet, DIP) provides more robustness to changes in input size, but they still do not provide satisfactory predictions at 8K resolution. Adaptive pyramids (RAPIDFlow, DPFlow) can counteract the resolution increase and stabilize the predictions, keeping a linear error increase according to the input size. DPFlow outperforms all other approaches at larger resolutions, surpassing RAPIDFlow by over 30% at 8K.

Resource management. Many top-performing methods cannot handle large 4K and 8K inputs with consumer hardware equipped with 24GB GPUs. Therefore, developing efficient methods for high-resolution inputs is necessary.

Input tiling. Cropping the input mitigates the memory overflow and somewhat stabilizes the predictions. However, cropping loses global information, leading to obvious square-shaped artifacts (see Fig. 1a) and significantly longer latencies at high resolutions.

Qualitative results. Figure 8 illustrates how the prediction of some methods changes with increasing resolution inputs. SEA-RAFT uses fixed-scale features, and it is significantly affected by high-resolution inputs. The tiling technique adopted by FlowFormer++ mitigates the problem to some extent, but the loss of global information causes noticeable degradation at 8K. RAPIDFlow shows relatively accurate results due to its adaptive pyramids, but its predictions miss important structural details. DPFlow maintains more stable results across all resolutions.

5.3. Standard-Resolution Evaluation

We also evaluate our model on the widely adopted MPI-Sintel [5] and KITTI 2015 [36] datasets, which contains

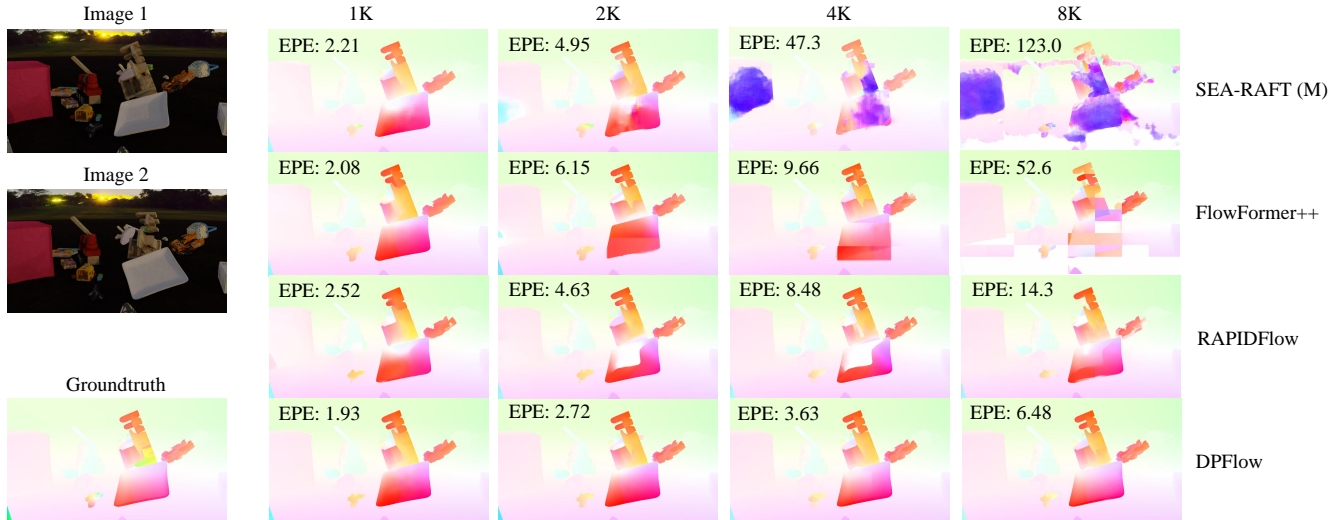


Figure 8. Qualitative results comparing the behavior of some optical flow methods when the input size grows from 1K to 8K resolution.

samples at around 1K resolution.

5.3.1. Public Benchmarks

We use the models trained with stages 3 and 4a to submit our results to the official public benchmarks. The results in Tab. 4 show that DPFlow can also achieve top-performing results in standard resolution. Among two-frame methods, we achieved the best average rank on the KITTI and Sintel benchmarks. Also, despite achieving remarkable results with its adaptive pyramid at higher resolutions, we observe that RAPIDFlow [38] underperforms at these standard benchmarks. DPFlow, on the other hand, shows consistent results in all evaluations, highlighting the benefits of our proposed approach.

5.3.2. Generalization

We evaluate the generalization capabilities using the model trained until stage two for a zero-shot evaluation on the selected benchmarks. Table 5 shows we also achieve remarkable generalization results. We outperform FlowDiffuser [33] and SEA-RAFT (L) [60] by 6% on the KITTI dataset. DPFlow is also only 3% behind the top-performing FlowDiffuser on the Sintel final pass.

5.4. Ablation Study

We conduct ablation studies to evaluate the design choices of our dual-pyramid encoder. We analyze the generalization results after stage 2 training with 100k iterations.

5.4.1. Encoder Structure

First, we assess the impact of our dual-pyramid structure and bidirectional recurrent unit. Table 6 shows that both choices improve the results on both benchmarks. The use of bidirectional GRU shows more significant improvements,

Table 4. Benchmark evaluation on MPI-Sintel and KITTI 2015 public test sets. The last column represents the average ranking on the three benchmarks.

Method	MPI-Sintel		KITTI 2015	Avg. rank
	clean	final	Fl-All	
RAPIDFlow [38]	2.03	3.56	6.12	21.0
RAFT [56]	1.60	2.85	5.10	19.3
GMA [23]	1.38	2.47	5.25	17.0
RPKNet [39]	1.31	2.65	4.64	15.7
DIP [68]	1.43	2.83	4.21	14.7
KPA-Flow [31]	1.35	2.36	4.60	13.0
SKFlow [54]	1.28	2.27	4.84	13.0
SEA-RAFT (L) [60]	1.31	2.60	4.30	12.7
DDVM [43]	1.75	2.47	3.26	11.7
MS-RAFT+ [20]	1.23	2.68	4.19	11.7
FlowFormer [15]	1.19	2.12	4.68	11.3
MatchFlow [10]	1.16	2.37	4.63	11.3
AnyFlow [24]	1.23	2.44	4.41	10.7
GMFlow+ [64]	1.03	2.37	4.49	8.0
CroCo-Flow [61]	1.09	2.44	3.64	7.3
GAFLOW [32]	1.15	2.05	4.42	7.3
FlowFormer++ [48]	1.07	1.94	4.52	6.3
SAMFlow [69]	1.00	2.08	4.49	5.7
CCMR+ [21]	1.07	2.10	3.86	5.0
FlowDiffuser [33]	<u>1.02</u>	2.03	4.17	<u>3.3</u>
DPFlow	1.04	<u>1.97</u>	<u>3.56</u>	2.7

highlighting the importance of bringing information from deeper features to shallower ones.

Table 5. Generalization results on MPI-Sintel and KITTI 2015 train sets.

Method	MPI-Sintel		KITTI 2015	
	clean	final	EPE	FI-All
RAFT [56]	1.44	2.71	5.04	17.4
GMA [23]	1.30	2.74	4.69	17.1
DIP [68]	1.30	2.82	4.29	13.7
FlowFormer [15]	0.95	2.35	4.09	14.7
GMFlowNet [67]	1.14	2.71	4.24	15.4
SKFlow [54]	1.22	2.46	4.47	15.5
AnyFlow [24]	1.10	2.52	3.76	12.4
FlowFormer++ [48]	<u>0.90</u>	2.30	3.93	14.1
GAFlow [32]	0.95	2.34	3.92	13.9
GMFlow+ [64]	<u>0.90</u>	2.74	5.74	17.6
MatchFlow [10]	1.03	2.45	4.08	15.6
CCMR+ [21]	0.98	2.36	-	12.8
RPKNet [39]	1.12	2.45	3.78	13.0
SEA-RAFT (L) [60]	1.19	4.11	<u>3.62</u>	12.9
FlowDiffuser [33]	0.86	2.19	-	<u>11.8</u>
DPFlow	1.02	<u>2.26</u>	3.37	11.1

5.4.2. Encoder Block

Next, we check how the CGU compares to other commonly adopted network blocks. Table 7 shows that CGU achieves the best generalization results on almost all benchmarks. In particular, we outperform the Swin Transformer [28] equipped with a cross-attention mechanism [63]. CGU also compares favorably against convolution-based approaches, such as ConvNeXt [29] and ResNet [13].

5.4.3. Pyramid Depth

DPFlow can adjust the pyramid depth at inference time to adapt to different inputs. Here, we study how the depth change affects the results. Table 8 shows the optimal number of levels is highly correlated to the input resolution, and the best results are usually obtained by adding another pyramid level when the input resolution doubles.

6. Conclusions

This paper addressed the current limitation of high-resolution optical flow estimation. Our proposed DPFlow adopted a dual-pyramid framework with a recurrent network to produce high-quality optical flow estimation at multiple input resolutions in a single model. Our experiments show that DPFlow achieves state-of-the-art results on multiple benchmarks, especially with high-resolution inputs.

We also created the Kubric-NK dataset containing annotated optical flow samples for resolutions ranging from 1K to 8K. This dataset provides a quantitative evaluation to compare the generalization capabilities to changes in in-

Table 6. Ablation on the encoder structure.

Dual Pyr.	Bidir.	MPI-Sintel		KITTI 2015	
		clean	final	EPE	FI-All
–	–	1.38	2.58	4.50	13.9
✓	–	1.38	2.51	4.70	13.7
✓	✓	1.35	2.41	4.13	12.1

Table 7. Ablation on the encoder block. FLOPs are calculated with a 1K-resolution input.

Encoder	MPI-Sintel		KITTI 2015		FLOP (G)
	clean	final	EPE	FI-All	
ResNet [13]	1.44	2.54	4.93	13.9	922
ConvNeXt [29]	1.33	2.50	4.34	13.3	674
Cross-Swin [63]	1.37	2.63	4.85	14.1	1187
CGU	1.35	2.41	4.13	12.1	778

Table 8. Average results with different pyramid levels.

Dataset	Metric	Pyr. levels			
		3	4	5	6
KITTI 2015 (1K)	FI-All ↓	11.1	11.7	11.7	12.7
MPI-Sintel (1K)	EPE ↓	1.65	1.71	1.86	1.88
Spring (2K)	1px ↓	3.56	3.53	3.60	3.71
VIPER (2K)	WAUC ↑	72.7	69.5	61.1	70.1
Mbury-ST (3K)	EPE ↓	16.8	7.47	5.09	5.27
Kubric-1K		0.50	0.53	0.59	0.61
Kubric-2K		0.92	0.85	0.86	1.04
Kubric-4K	EPE ↓	2.57	1.80	1.77	1.81
Kubric-8K		14.7	5.97	4.37	4.11

put size. Our high-resolution study provides new insights into designing more robust optical flow methods. In particular, adaptive pyramids showed a significant advantage in counteracting the input size changes and providing stable predictions at all resolutions. At high resolutions, DPFlow outperformed all previous methods by large margins.

Limitations. DPFlow achieves comparable or superior results in almost all evaluations except the MPI-Sintel clean pass subset. This subset contains synthetic images rendered without adverse conditions, such as motion blur and fog. Therefore, other methods can still provide better accuracy when handling clean images at standard resolutions. The proposed Kubric-NK dataset does not evaluate the effects of other conditions, such as lighting, fog, and fine details. Combining adversary conditions with high-resolution annotated inputs remains an open topic.

7. Acknowledgments

This research is supported by the National Science Fund for Distinguished Young Scholars (62125601), the Beijing Natural Science Foundation (IS23060), the National Natural Science Foundation of China (62172035), the Youth Teacher International Exchange & Growth Program (No. QNXM20250001), and the Fundamental Research Funds for the Central Universities (FRF-TP-2021-01C2, FRF-TP-22-048A1). RMCJ is grateful to FAPESP (grants #2022/15304-4), USP - UGPN, CNPq, CAPES, FINEP, and MCTI PPI-SOFTEX (TIC 13 DOU 01245.010222/2022-44).

References

- [1] Nicolas Ballas, L. Yao, Christopher Joseph Pal, and Aaron C. Courville. Delving deeper into convolutional networks for learning video representations. In *ICLR*, 2016. 3
- [2] Connelly Barnes, Eli Shechtman, Adam Finkelstein, and Dan B. Goldman. PatchMatch: a randomized correspondence algorithm for structural image editing. *ToG*, 28(3): 24, 2009. 2
- [3] Thomas Brox and Jitendra Malik. Large displacement optical flow: Descriptor matching in variational motion estimation. *TPAMI*, 33:500–513, 2011. 2
- [4] Thomas Brox, Andrés Bruhn, Nils Papenberg, and Joachim Weickert. High accuracy optical flow estimation based on a theory for warping. In *ECCV*, pages 25–36. Springer, 2004. 2
- [5] D. J. Butler, J. Wulff, G. B. Stanley, and M. J. Black. A naturalistic open source movie for optical flow evaluation. In *ECCV*, pages 611–625, 2012. 2, 3, 5, 6, 13
- [6] Haiyang Chao, Yu Gu, and Marcello Rosario Napolitano. A survey of optical flow techniques for robotics navigation applications. *J. Intell. Robot. Syst.*, 73:361–372, 2014. 1
- [7] Yann Dauphin, Angela Fan, Michael Auli, and David Grangier. Language modeling with Gated Convolutional Networks. In *ICML*, pages 933–941, 2017. 4
- [8] Carl Doersch, Ankush Gupta, Larisa Markeeva, Adria Recasens, et al. TAP-Vid: A benchmark for tracking any point in a video. In *NeurIPS Datasets Track*, 2022. 2, 3
- [9] Qiaole Dong and Yanwei Fu. MemFlow: Optical flow estimation and prediction with memory. In *CVPR*, 2024. 2, 6
- [10] Qiaole Dong, Chenjie Cao, and Yanwei Fu. Rethinking optical flow from geometric matching consistent perspective. In *CVPR*, pages 1337–1347, 2023. 2, 6, 7, 8, 14, 18
- [11] Alexey Dosovitskiy, Philipp Fischer, Eddy Ilg, Philip Hausser, et al. FlowNet: learning optical flow with convolutional networks. In *ICCV*, pages 2758–2766, 2015. 2, 3, 5, 13
- [12] Klaus Greff, Francois Belletti, Lucas Beyer, Carl Doersch, et al. Kubric: A scalable dataset generator. In *CVPR*, pages 3739–3751, 2022. 4, 15
- [13] Kaiming He, X. Zhang, Shaoqing Ren, and Jian Sun. Deep residual learning for image recognition. *CVPR*, pages 770–778, 2016. 8
- [14] Dan Hendrycks and Kevin Gimpel. Gaussian Error Linear Units (GELUs). *ArXiv*, 2016. 4
- [15] Zhaoyang Huang, Xiaoyu Shi, Chao Zhang, Qiang Wang, et al. FlowFormer: A transformer architecture for optical flow. In *ECCV*, pages 668–685, 2022. 2, 3, 6, 7, 8, 14
- [16] Tak-Wai Hui, Xiaoou Tang, and Chen Change Loy. LiteFlowNet: a lightweight convolutional neural network for optical flow estimation. In *CVPR*, pages 8981–8989, 2018. 2
- [17] Junhwa Hur and Stefan Roth. Iterative residual refinement for joint optical flow and occlusion estimation. In *CVPR*, pages 5754–5763, 2019. 6
- [18] Md Amirul Islam, Matthew Kowal, Sen Jia, Konstantinos G Derpanis, and Neil DB Bruce. Position, padding and predictions: A deeper look at position information in CNNs. *IJCV*, pages 1–22, 2024. 4
- [19] Andrew Jaegle, Sebastian Borgeaud, Jean-Baptiste Alayrac, Carl Doersch, et al. Perceiver IO: a general architecture for structured inputs & outputs. In *ICLR*, 2022. 2, 3, 6, 14
- [20] Azin Jahedi, Maximilian Luz, Marc Rivinius, Lukas Mehl, and Andrés Bruhn. MS-RAFT+: High resolution Multi-Scale RAFT. *IJCV*, 2023. 6, 7, 14
- [21] Azin Jahedi, Maximilian Luz, Marc Rivinius, and Andrés Bruhn. CCMR: High resolution optical flow estimation via coarse-to-fine context-guided motion reasoning. In *WACV*, 2024. 6, 7, 8, 14
- [22] Joel Janai, Fatma Güney, Jonas Wulff, Michael J. Black, and Andreas Geiger. Slow Flow: Exploiting high-speed cameras for accurate and diverse optical flow reference data. In *CVPR*, pages 1406–1416, 2017. 3
- [23] Shihao Jiang, Dylan Campbell, Yao Lu, Hongdong Li, and Richard Hartley. Learning to estimate hidden motions with global motion aggregation. In *ICCV*, pages 9752–9761, 2021. 1, 2, 6, 7, 8, 14, 18
- [24] Hyunyoung Jung, Zhuo Hui, Lei Luo, Haitao Yang, et al. AnyFlow: Arbitrary scale optical flow with implicit neural representation. In *CVPR*, pages 5455–5465, 2023. 7, 8
- [25] Daniel Kondermann, Rahul Nair, Katrin Honauer, Karsten Krispin, et al. The HCI benchmark suite: Stereo and flow ground truth with uncertainties for urban autonomous driving. In *CVPR Workshops*, pages 19–28, 2016. 2, 3, 5, 13
- [26] Nihal Kumar, Om Prakash Verma, and Anil Singh Parihar. Evolution of transformer-based optical flow estimation techniques: a survey. *Multimedia Tools and Applications*, pages 1–42, 2024. 2
- [27] Jing Lin, Xiaowan Hu, Yuanhao Cai, Haoqian Wang, et al. Unsupervised flow-aligned sequence-to-sequence learning for video restoration. In *ICML*, pages 13394–13404. PMLR, 2022. 1
- [28] Ze Liu, Yutong Lin, Yue Cao, Han Hu, et al. Swin Transformer: Hierarchical Vision Transformer using Shifted Windows. In *ICCV*, pages 10012–10022, 2021. 8
- [29] Zhuang Liu, Hanzi Mao, Chao-Yuan Wu, Christoph Feichtenhofer, et al. A ConvNet for the 2020s. In *CVPR*, pages 11966–11976, 2022. 8
- [30] Yawen Lu, Qifan Wang, Siqi Ma, Tong Geng, et al. TransFlow: Transformer as flow learner. In *CVPR*, pages 18063–18073, 2023. 2

- [31] Ao Luo, Fan Yang, Xin Li, and Shuaicheng Liu. Learning optical flow with kernel patch attention. In *CVPR*, pages 8896–8905, 2022. 7
- [32] Ao Luo, F. Yang, Xin Li, Lang Nie, et al. GAFlow: Incorporating gaussian attention into optical flow. In *ICCV*, pages 9642–9651, 2023. 2, 7, 8
- [33] Ao Luo, Xin Li, Fan Yang, Jiangyu Liu, et al. FlowDiffuser: Advancing optical flow estimation with diffusion models. In *CVPR*, pages 19167–19176, 2024. 7, 8
- [34] N. Mayer, E. Ilg, P. Häusser, P. Fischer, et al. A large dataset to train convolutional networks for disparity, optical flow, and scene flow estimation. In *CVPR*, pages 4040–4048, 2016. 3, 5, 13
- [35] Lukas Mehl, Jenny Schmalfluss, Azin Jahedi, Yaroslava Naliwayko, and Andrés Bruhn. Spring: A high-resolution high-detail dataset and benchmark for scene flow, optical flow and stereo. In *CVPR*, pages 4981–4991, 2023. 1, 2, 3, 5, 12, 13, 14
- [36] Moritz Menze and Andreas Geiger. Object scene flow for autonomous vehicles. In *CVPR*, pages 3061–3070, 2015. 1, 2, 3, 5, 6, 12, 13
- [37] Henrique Morimitsu. Pytorch lightning optical flow. <https://github.com/hmorimitsu/ptlflow>, 2021. 5
- [38] Henrique Morimitsu, Xiaobin Zhu, Roberto M. Cesar-Jr, Xiangyang Ji, and Xu-Cheng Yin. RAPIDFlow: Recurrent Adaptable Pyramids with Iterative Decoding for efficient optical flow estimation. In *JCR*, 2024. 1, 2, 3, 6, 7, 18
- [39] Henrique Morimitsu, Xiaobin Zhu, Xiangyang Ji, and Xu-Cheng Yin. Recurrent partial kernel network for efficient optical flow estimation. In *AAAI*, pages 4278–4286, 2024. 2, 3, 6, 7, 8, 14, 18
- [40] Jordi Pont-Tuset, Federico Perazzi, Sergi Caelles, Pablo Arbeláez, et al. The 2017 DAVIS challenge on video object segmentation. *ArXiv*, 2017. 1, 18, 20
- [41] Anurag Ranjan and Michael J. Black. Optical flow estimation using a spatial pyramid network. In *CVPR*, pages 4161–4170, 2017. 2
- [42] Stephan R. Richter, Zeeshan Hayder, and Vladlen Koltun. Playing for benchmarks. In *ICCV*, pages 2232–2241, 2017. 3, 5, 12, 13
- [43] Saurabh Saxena, Charles Herrmann, Junhwa Hur, Abhishek Kar, et al. The surprising effectiveness of diffusion models for optical flow and monocular depth estimation. In *NeurIPS*, 2023. 7
- [44] Daniel Scharstein, Heiko Hirschmüller, York Kitajima, Greg Krathwohl, et al. High-resolution stereo datasets with subpixel-accurate ground truth. In *GCPR*, pages 31–42. Springer, 2014. 3, 5, 13, 14, 17, 18, 21
- [45] Wonyong Seo, Woonsung Park, and Munchurl Kim. Lightweight optical flow estimation using 1D matching. *IEEE Access*, 12:45560–45571, 2024. 4
- [46] Laura Sevilla-Lara, Yiyi Liao, Fatma Güney, Varun Jampani, et al. On the integration of optical flow and action recognition. In *GCPR*, pages 281–297. Springer, 2018. 1
- [47] Xiaoyu Shi, Zhaoyang Huang, Weikang Bian, Dasong Li, et al. VideoFlow: Exploiting temporal cues for multi-frame optical flow estimation. In *ICCV*, pages 12469–12480, 2023. 2
- [48] Xiaoyu Shi, Zhaoyang Huang, Dasong Li, Manyuan Zhang, et al. FlowFormer++: Masked cost volume autoencoding for pretraining optical flow estimation. In *CVPR*, pages 1599–1610, 2023. 1, 2, 6, 7, 8, 14, 18
- [49] Maria Shugrina, Ziheng Liang, Amlan Kar, Jiaman Li, et al. Creative flow+ dataset. In *CVPR*, 2019. 2, 3
- [50] Hyeonjun Sim, Jihyong Oh, and Munchurl Kim. XVFI: eXtreme Video Frame Interpolation. In *ICCV*, pages 14469–14478, 2021. 2
- [51] Deqing Sun, Xiaodong Yang, Ming-Yu Liu, and Jan Kautz. PWC-Net: CNNs for optical flow using pyramid, warping, and cost volume. In *CVPR*, pages 8934–8943, 2018. 2, 6
- [52] Guolei Sun, Yun Liu, Henghui Ding, Thomas Probst, and Luc Van Gool. Coarse-to-fine feature mining for video semantic segmentation. In *CVPR*, pages 3126–3137, 2022. 2
- [53] Jiaming Sun, Zehong Shen, Yuang Wang, Hujun Bao, and Xiaowei Zhou. LoFTR: Detector-free local feature matching with transformers. In *CVPR*, pages 8922–8931, 2021. 3
- [54] Shangkun Sun, Yuanqi Chen, Y. Zhu, Guodong Guo, and Gezhong Li. SKFlow: Learning optical flow with super kernels. In *NeurIPS*, 2022. 6, 7, 8, 14, 18
- [55] Chuanbo Tang, Xihua Sheng, Zhuoyuan Li, Haotian Zhang, Li Li, and Dong Liu. Offline and online optical flow enhancement for deep video compression. In *AAAI*, pages 5118–5126, 2024. 1
- [56] Zachary Teed and Jia Deng. RAFT: recurrent all-pairs field transforms for optical flow. In *ECCV*, pages 402–419, 2020. 2, 6, 7, 8, 14, 18
- [57] Hugo Touvron, Matthieu Cord, Alexandre Sablayrolles, Gabriel Synnaeve, and Hervé Jégou. Going deeper with image transformers. In *ICCV*, pages 32–42, 2021. 4
- [58] Ashish Vaswani, Noam Shazeer, Niki Parmar, Jakob Uszkoreit, et al. Attention Is All You Need. In *NeurIPS*, page 6000–6010, 2017. 1, 2, 3
- [59] Wenshan Wang, DeLong Zhu, Xiangwei Wang, Yaoyu Hu, et al. TartanAir: A dataset to push the limits of visual SLAM. In *IROS*, pages 4909–4916, 2020. 3
- [60] Yihan Wang, Lahav Lipson, and Jia Deng. SEA-RAFT: Simple, Efficient, Accurate RAFT for optical flow. In *ECCV*, 2024. 1, 2, 4, 5, 6, 7, 8, 12, 14, 18
- [61] Philippe Weinzaepfel, Thomas Lucas, Vincent Leroy, Yann Cabon, et al. CroCo v2: Improved cross-view completion pre-training for stereo matching and optical flow. In *ICCV*, pages 17969–17980, 2023. 2, 5, 6, 7, 17, 18
- [62] Haofei Xu, Jiaolong Yang, Jianfei Cai, Juyong Zhang, and Xin Tong. High-resolution optical flow from 1D attention and correlation. In *ICCV*, pages 10478–10487, 2021. 2, 4, 5, 17
- [63] Haofei Xu, Jing Zhang, Jianfei Cai, Hamid Rezaatofghi, and Dacheng Tao. GMFlow: Learning optical flow via global matching. In *CVPR*, pages 8121–8130, 2022. 1, 2, 3, 6, 8
- [64] Haofei Xu, Jing Zhang, Jianfei Cai, Hamid Rezaatofghi, et al. Unifying flow, stereo and depth estimation. *TPAMI*, 45(11): 13941–13958, 2023. 2, 6, 7, 8, 14, 18

- [65] Gengshan Yang and Deva Ramanan. Volumetric correspondence networks for optical flow. In *NeurIPS*, pages 793–803, 2019. [6](#)
- [66] Shi-Xue Zhang, Chun Yang, Xiaobin Zhu, and Xu-Cheng Yin. Arbitrary shape text detection via boundary transformer. *TMM*, 26:1747–1760, 2023. [2](#)
- [67] Shiyu Zhao, Long Zhao, Zhixing Zhang, Enyu Zhou, and Dimitris N. Metaxas. Global matching with overlapping attention for optical flow estimation. In *CVPR*, pages 17571–17580, 2022. [1](#), [2](#), [8](#)
- [68] Zihua Zheng, Ni Nie, Zhi Ling, Pengfei Xiong, et al. DIP: Deep inverse patchmatch for high-resolution optical flow. In *CVPR*, pages 8915–8924, 2022. [2](#), [4](#), [5](#), [6](#), [7](#), [8](#), [14](#), [18](#)
- [69] Shili Zhou, Ruian He, Weimin Tan, and Bo Yan. SAMFlow: Eliminating any fragmentation in optical flow with segment anything model. In *AAAI*, 2024. [7](#)

DPFlow: Adaptive Optical Flow Estimation with a Dual-Pyramid Framework

Supplementary Material

8. Training and evaluation details

Table 9 shows the hyperparameters we used during each training stage.

9. Checkpoint results

We report the results of our model after each of the four training stages in Tab. 10. These results can be used as a sanity check to reproduce the training of our model.

10. Model details

Table 11 details different models’ size, time, and memory costs with input resolutions ranging from 1K to 8K. Due to deep feature pyramids, DPFlow has low computational costs and offers relatively low latency, being faster than most top-performing methods. FlowFormer++ and MatchFlow can reduce memory consumption using input tiling, but this strategy increases inference time considerably. RP-KNet can achieve lower computational costs, but DPFlow offers a 23% improvement on the KITTI 2015 benchmark.

11. Evaluation details

11.1. Metrics

This section explains how to calculate the metrics we use for the evaluations in each benchmark. Let $F \in \mathbb{R}^{N \times 2}$ be the predicted flow and $G \in \mathbb{R}^{N \times 2}$ the groundtruth, where $N = HW$ for height H and width W . Then, the metrics are calculated as follows.

End-Point-Error (EPE): consists of the average Euclidean distance between the predicted flow vectors and the groundtruth ones:

$$\text{EPE}(F, G) = \frac{1}{N} \sum_{i=1}^N \|F_i - G_i\|_2. \quad (3)$$

Outlier ratio: represents the percentage of predictions whose Euclidean distances are beyond a given threshold τ :

$$\text{Outlier}(F, G) = \frac{1}{N} \sum_{i=1}^N [\|F_i - G_i\|_2 > \tau], \quad (4)$$

where $[\cdot]$ is the Iverson bracket. Each benchmark selects a specific threshold value and represents its metric by a different name. For example, the KITTI benchmark [36] adopts $\tau = \max(3, 0.05\|G_i\|_2)$ and calls their metric **FI-All**. On the other hand, the Spring benchmark [35] uses $\tau = 1$ and names their metric as **1px**.

Weighted Area Under the Curve (WAUC): used by the VIPER dataset [42] to integrate over multiple thresholds and give more importance to more accurate results.

$$\text{WAUC}(F, G) = \frac{100}{N \sum_{i=1}^{100} w_i} \sum_{i=1}^{100} w_i \sum_{j=1}^N [\|F_j - G_j\|_2 \leq \delta_i], \quad (5)$$

where $[\cdot]$ is the Iverson bracket, $\delta_i = \frac{i}{20}$ and $w_i = 1 - \frac{i-1}{100}$.

11.2. Spring dataset metrics

To improve the evaluation of predictions for very thin structures, the Spring benchmark [35] proposed to generate the groundtruth at doubled resolution (image is 2K and groundtruth is 4K). Therefore, each prediction (at 2K) is compared with its four corresponding groundtruth values at 4K, and the lowest error is chosen as the metric. We follow the same procedure when evaluating the train results at 2K in Tab. 3 in the main paper. Unlike the study by SEARAFT [60], we also use the images at full resolution instead of downsampling them to 1K, which explains the difference in our results.

For the Spring train 4K evaluation in Tab. 3 in the main paper, we use bicubic interpolation to upsample the images from 2K to 4K. We also double the flow groundtruth values since they are originally encoded for a 2K resolution evaluation. Since the upsampling may create artifacts at the motion boundaries, we create a mask to ignore pixels near the borders. We create this mask using a strategy similar to the one the authors proposed for handling thin structures. We first reduce the 4K groundtruth to 2K resolution by stacking 2×2 pixel blocks. Then, we calculate the EPE metric between all combinations of the four pixels inside each 2×2 block. If the maximum EPE within a block is greater than one, we consider this block to lie on a motion boundary and ignore all four pixels. The Python code describing this procedure is shown in Listing 1.

12. Choosing the evaluation checkpoint

Here, we include the individual results for each method we used to calculate the averages presented in Tab. 2 in the main paper.

12.1. Spring dataset

Due to the large size of the Spring dataset [35], we only use the first 10% samples from each sequence for this experiment (480 samples). The results are presented in Tab. 12.

Table 9. Hyperparameters for each training stage. Batch sizes $\times 4$ indicate that gradients were accumulated during 4 iterations before backpropagating. Dataset abbreviations denote C: FlyingChairs [11], T: FlyingThings3D [34], H: HD1K [25], S: Sintel [5], K: KITTI 2015 [36], Sp: Spring [35].

Stage	Datasets	Batch	Iters (Epochs)	LR	WD	GPU hrs.
1	C	10	100k (45)	2.5×10^{-4}	10^{-4}	70
2	T	6	1M (80)	1.25×10^{-4}	10^{-4}	700
3	T+H+S+K	6×4	120k (25)	1.25×10^{-4}	10^{-5}	300
4a	K	6	2k (250)	1×10^{-4}	10^{-5}	6
4b	Sp	4×4	120k (100)	1×10^{-4}	10^{-5}	360

Table 10. Results after each training stage. Values in parentheses indicate that the same dataset was used during training.

Stage	S. Clean	S. Final	KITTI 2015	
	EPE	EPE	EPE	Fl-All
1	2.74	3.91	11.1	32.1
2	1.02	2.26	3.37	11.1
3	(0.55)	(0.86)	(1.04)	(3.18)
4a	0.80	1.24	(0.83)	(2.24)
4b	1.37	2.45	6.36	15.7

12.2. VIPER dataset

Due to the large size of the VIPER dataset [42], we only use the first 10% samples from each sequence for this experiment (473 samples). The results are presented in Tab. 13.

12.3. Middlebury-ST dataset

We use all 23 training samples of the Middlebury-ST dataset [44] for this experiment. The results are presented in Tab. 14.

12.4. Kubric-1K dataset

We use all 600 samples at 1K resolution from our proposed Kubric-NK dataset for this experiment. The results are presented in Tab. 15.

13. Feature visualization

We study the activation patterns of the CGU cross-gate to see what type of pattern they focus on. Here, we select the output feature of the encoder network and save the gate activations using heatmaps. Figures 9 and 10 show the gate activations on samples from the Kubric-NK (8K resolution) and KITTI 2015 (1K), respectively. We observe that some gates can capture some structural information about the scene. For example, some channels focus on horizontal and vertical lines, while others separate background from foreground and encode motion boundaries.

Listing 1. Python code for masking out pixels on the motion boundaries to calculate the metric for the Spring train 4K evaluation in Tab. 3 in the main paper.

```

import torch
import torch.nn.functional as F
from einops import rearrange

def compute_valid_mask(flow: torch.Tensor):
    # flow shape is [B, 2, H, W]
    # downsample by stacking 2x2 blocks
    flow_stack = rearrange(
        flow,
        "b c (h nh) (w nw) -> b (nh nw) c h w",
        nh=2,
        nw=2
    )
    # calculate EPE between all pairs
    # in each 2x2 block
    flow_stack4 = flow_stack.repeat(
        1, 4, 1, 1, 1)
    flow_stack4 = rearrange(
        flow_stack4,
        "b (m n) c h w -> b m n c h w",
        m=4)
    diff = flow_stack[:, :, None] - flow_stack4
    diff = rearrange(
        diff,
        "b m n c h w -> b (m n) c h w"
    )
    diff = torch.sqrt(torch.pow(diff, 2).sum(2))
    # mark pixels as valid only if the maximum
    # EPE of their block is below one
    max_diff, _ = diff.max(1)
    max_diff = F.interpolate(
        max_diff[:, None],
        scale_factor=2,
        mode="nearest"
    )
    valid_mask = max_diff < 1.0
    return valid_mask

```

14. Input downsampling

One popular strategy to avoid handling high-resolution inputs consists of first downsampling the inputs and then up-sampling the predictions back to the original resolution. Here, we conduct a study to evaluate how this input down-

Table 11. Model details. \square denotes methods that use input tiling [15, 19]. * indicates that the model is running in local correlation mode, which decreases memory consumption but increases inference time. † results are not available due to running out of memory. Times are calculated using an NVIDIA RTX3090 GPU.

Model	KITTI 2015 (Fl-All)	Params (M)	Time (s)				Memory (GB)			
			1K	2K	4K	8K	1K	2K	4K	8K
RAFT [56]*	5.10	<u>5.25</u>	0.51	1.36	4.76	†	<u>0.65</u>	1.71	6.40	†
GMA [23]	5.25	5.88	0.18	1.17	†	†	1.41	17.3	†	†
DIP [68]	4.21	5.37	0.51	2.11	8.60	†	1.59	5.46	20.9	†
SKFlow [54]	4.84	6.27	0.31	1.70	†	†	1.17	17.4	†	†
FlowFormer++ [48] \square	4.52	16.1	1.17	2.68	9.02	29.9	4.24	4.37	6.10	<u>18.7</u>
MatchFlow [10] \square	4.63	15.4	0.63	1.44	5.82	22.8	1.31	<u>1.61</u>	3.04	<u>20.7</u>
MS-RAFT+ [20]*	4.19	16.1	0.74	2.82	†	†	2.61	9.34	†	†
GMFlow+ [64]	4.49	7.36	0.23	1.69	†	†	2.99	20.6	†	†
RPKNet [39]*	4.64	2.84	0.08	0.28	1.18	5.34	0.56	1.34	<u>4.42</u>	16.8
SEA-RAFT (L) [60]*	4.30	19.6	0.24	0.70	2.60	†	0.79	2.02	7.21	†
CCMR+ [21]*	3.86	11.5	1.34	5.36	†	†	3.19	12.1	†	†
DPFlow*	3.56	10.0	<u>0.16</u>	<u>0.53</u>	<u>1.98</u>	<u>8.40</u>	0.76	1.90	6.70	20.7

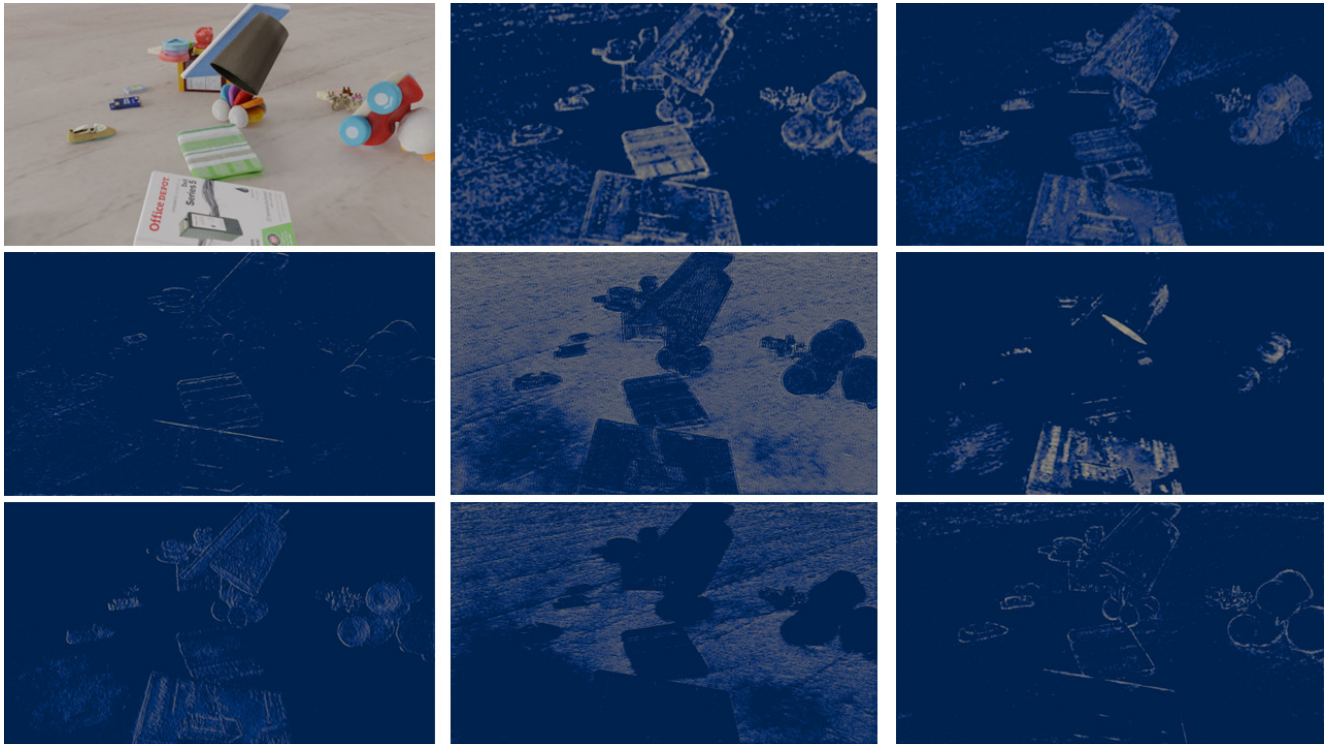


Figure 9. Visualization of cross-gate activations on an 8K sample from the Kubric-NK dataset.

sampling affects the results. We use samples from three high-resolution datasets: Spring [35] (2K), Middlebury-ST [44] (3K), and Kubric-NK (8K). For this study, we use bilinear interpolation to first downsample the inputs to 1K resolution, and then upsample the predictions back to the original sizes before computing the accuracy metrics.

The results in Tab. 16 show some interesting observations. Downsampling from 2K to 1K in the Spring benchmark negatively impacts all methods except GMFlow+. This result indicates that most approaches are robust to this input size, but the global matching strategy from GMFlow+ may have more bias towards the training sizes. On the

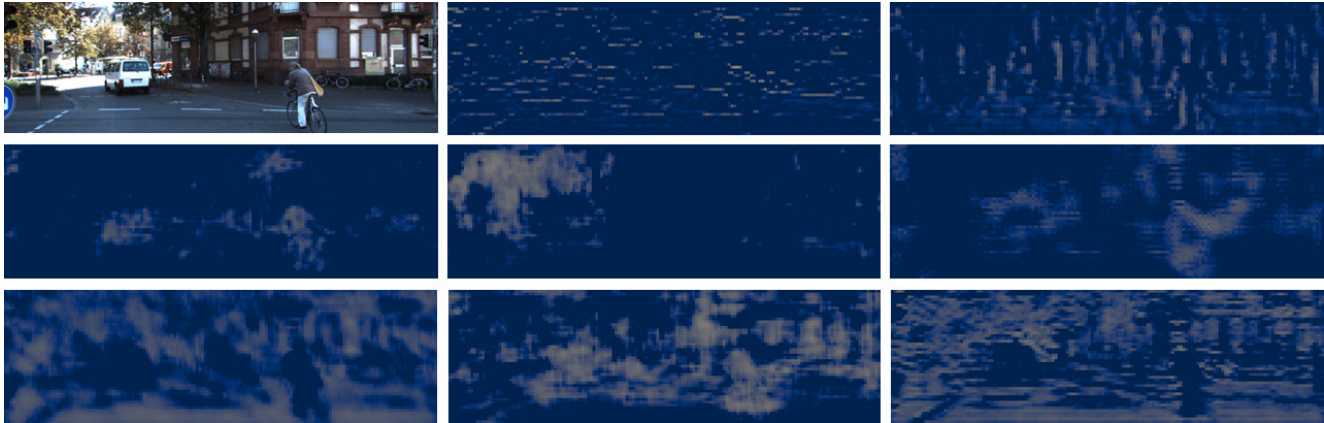


Figure 10. Visualization of cross-gate activations on a 1K sample from the KITTI 2015 dataset.

Table 12. Training stage experiments on the Spring dataset.

Method	1px ↓	
	Stage 2	Stage 3
PWC-Net	7.18	5.15
IRR	5.46	4.52
VCN	7.53	8.08
RAFT	4.45	3.85
GMA	4.33	3.67
DIP	4.36	4.21
GMFlow	5.92	6.83
FlowFormer	4.16	3.93
SKFlow	4.61	3.93
FlowFormer++	4.1	4.21
MatchFlow	4.33	4.15
GMFlow+	5.04	5.07
RPKNet	3.95	3.86
SEA-RAFT (M)	4.37	3.63
RAPIDFlow	4.32	3.94
DPFlow	4.76	3.53
Average	4.92	4.53

Table 13. Training stage experiments on the VIPER dataset.

Method	WAUC ↑	
	Stage 2	Stage 3
PWC-Net	51.2	61.3
IRR	58.1	61.4
VCN	55.6	58.4
RAFT	63.7	67.1
GMA	64	67.7
DIP	66.8	67.7
GMFlow	52.9	52.4
FlowFormer	66.1	68.8
SKFlow	64.4	67.8
FlowFormer++	66.8	68.6
MatchFlow	66.3	69.0
GMFlow+	64.8	65.8
RPKNet	66.9	68.7
SEA-RAFT (M)	68.9	71.8
RAPIDFlow	62.7	66.5
DPFlow	70.4	72.7
Average	63.1	65.9

Middlebury-ST 3K samples, we observe significant improvements in methods with fixed structures. On the other hand, adaptable methods like DPFlow and RAPIDFlow still benefit from processing the images at the original resolution. Using an eight-times downsampling on Kubric-NK benefits almost all methods. However, these results may be caused by the relatively simple shapes and motions generated by Kubric [12]. Since the objects do not present fine-grained details, downsampling them does not affect the input contents significantly. A more thorough study of the effects of downsampling would require a high-resolution dataset with finer and more complex motion patterns.

15. Kubric-NK

This section details the Kubric-NK dataset and presents additional discussions about the effect of input resolution on the performance of optical flow methods.

15.1. Dataset samples

Figure 11 shows an image pair and its respective optical flow annotation for each of the 30 sequences of the Kubric-NK dataset.

Table 14. Training stage experiments on the Middlebury-ST dataset.

Method	EPE ↓	
	Stage 2	Stage 3
PWC-Net	35.9	74.3
IRR	15.2	61.4
VCN	44.2	51
RAFT	35.2	51
DIP	16.7	21.2
FlowFormer	19.0	13.8
FlowFormer++	17.5	15.2
MatchFlow	16.7	19.4
RPKNet	15.0	16.4
SEA-RAFT (M)	65.1	59.2
RAPIDFlow	6.41	7.33
DPFlow	4.82	5.25
Average	24.3	32.9

Table 15. Training stage experiments on the Kubric-1K dataset.

Method	EPE ↓	
	Stage 2	Stage 3
PWC	1.4	1.28
IRR	0.95	1.1
VCN	1.23	1.09
RAFT	0.73	0.69
GMA	0.7	0.67
DIP	0.71	0.68
GMFlow	0.68	0.88
FlowFormer	0.5	0.52
SKFlow	0.69	0.62
FlowFormer++	0.48	0.46
MatchFlow	0.54	0.54
GMFlow+	0.48	0.45
MemFlow	0.57	0.55
SEA-RAFT(M)	0.56	0.53
RPKNet	0.61	0.6
RAPIDFlow	0.85	0.81
DPFlow	0.57	0.5
Average	0.72	0.70

15.2. Generalization to different resolutions

Optical flow estimation is fundamentally a point-matching problem between a pair of images. Therefore, the overall magnitude of the flow (correspondence) vectors tends to correlate with the size of the inputs, making it more difficult for higher-resolution inputs. There are two main optical flow estimation approaches: global and local matching.

Global matching can theoretically handle changes in the input size and large motions. However, the cost of global search increases quadratically according to the input size, which makes it unfeasible for larger inputs. Local matching only searches for correspondences within a limited window (typically 9×9) around the origin point. This approach, however, requires the corresponding points to be within the range of the search window. This causes a problem for most local methods because they adopt an encoder with a fixed structure, which makes the size of the feature directly determined by the input resolution. Figure 12 illustrates how the increase in input size affects the matching procedure and how DPFlow’s recurrent encoder alleviates this problem.

15.2.1. Training bias

Besides the problems caused by the limited search range, the training distribution also heavily affects the performance of non-adaptive models to different inputs. We demonstrate the effect of training bias with two studies based on the open-source models Flow1D [62] and CroCo [61].

Flow1D provides an additional model variant trained using a dataset with high-resolution samples. We compare the performance of Flow1D on Kubric-NK using the standard (trained for MPI-Sintel) and high-resolution training in Tab. 17. The results demonstrate that high-resolution training is effective and necessary to produce stable predictions at 4K resolution. However, we also observe that it negatively affects the results at the lower 1K resolution, thus clearly showing the effect of the training bias.

Our second study evaluates the performance of the CroCo model on the training split of the Middlebury v3 stereo-matching benchmark [44]. This benchmark contains 15 image pairs ranging from 1K to 3K resolution inputs. Since stereo-matching can be viewed as a subset of optical flow (matching only on the horizontal axis), optical flow models can be used for this task by zeroing the y-axis prediction. We chose the CroCo model because it provides trained variants for stereo and optical flow tasks using a common backbone network. The only differences between these variants are the number of output prediction heads (1 for stereo vs. 2 for optical flow) and the training samples.

Table 18 shows how using these two variants affects the Middlebury v3 training benchmark results. Although optical flow and stereo matching are both similar matching problems, directly transferring the optical flow-trained model for stereo estimation results in a noticeable degradation. Since both variants share the same architecture, these results further illustrate the effect of the training bias.

These studies demonstrated that the problems of handling different inputs can be mitigated with specialized training. In particular, training different variants for particular input resolutions can result in significant improvements. Nonetheless, this strategy is only palliative since it can only shift the problem to another resolution range. Moreover,

Table 16. Results on high-resolution benchmarks with and without downsampling the inputs. The @1K columns indicate that the inputs are downsampled to 1K resolution and the predictions are upsampled back to the original sizes. † results are not available due to running out of memory.

Method	Spring (1px ↓)		Mbury-ST (EPE ↓)		Kubric-NK (EPE ↓)	
	2K	@1K	3K	@1K	8K	@1K
RAFT [56]	3.85	4.52	35.2	8.01	82.7	5.09
GMA [23]	3.75	4.53	†	8.23	†	4.91
DIP [68]	3.64	3.87	16.7	8.01	†	5.42
SKFlow [54]	3.79	4.20	†	6.88	†	4.72
FlowFormer++ [48]	3.76	4.21	17.5	6.93	24.4	3.39
MatchFlow [10]	3.97	4.21	16.7	7.18	29.0	3.89
GMFlow+ [64]	5.72	4.00	†	<u>5.67</u>	†	4.43
RPKNet [39]	<u>3.28</u>	4.12	15.0	6.74	18.2	4.59
SEA-RAFT (M) [60]	3.47	3.53	65.1	6.71	51.8	4.07
RAPIDFlow [38]	3.73	5.06	<u>6.41</u>	8.99	<u>5.96</u>	5.99
DPFlow	3.06	<u>3.57</u>	5.09	5.63	4.13	<u>3.88</u>

Table 17. Flow1D results using standard-resolution stage 3 training (for MPI-Sintel benchmark) and after high-resolution re-training.

Train resolution	Kubric-NK (EPE ↓)		
	1K	2K	4K
Standard (Sintel)	0.85	1.80	32.7
High-res.	0.88	1.42	4.49

Table 18. Results of evaluating CroCo [61] variants trained on stereo and optical flow samples on the Middlebury v3 stereo matching benchmark.

Variant	Middlebury v3 (training)		
	EPE ↓	1px ↓	2px ↓
CroCo-Stereo	0.37	3.86	1.93
CroCo-Flow	7.17	29.7	20.1

training multiple variants of each model is expensive, especially with high-resolution inputs. One advantage of the proposed DPFlow is that it significantly reduces the input resolution gap by changing its pyramids on the fly without requiring additional training.

15.3. Additional qualitative results

This section shows some additional qualitative results of DPFlow on some high-resolution inputs. We demonstrate results on samples at 4K resolution from DAVIS [40] in Fig. 13, 3K from Middlebury-ST [44] in Fig. 14, and 1K to 8K from Kubric-NK in Figs. 15, 16, 17.

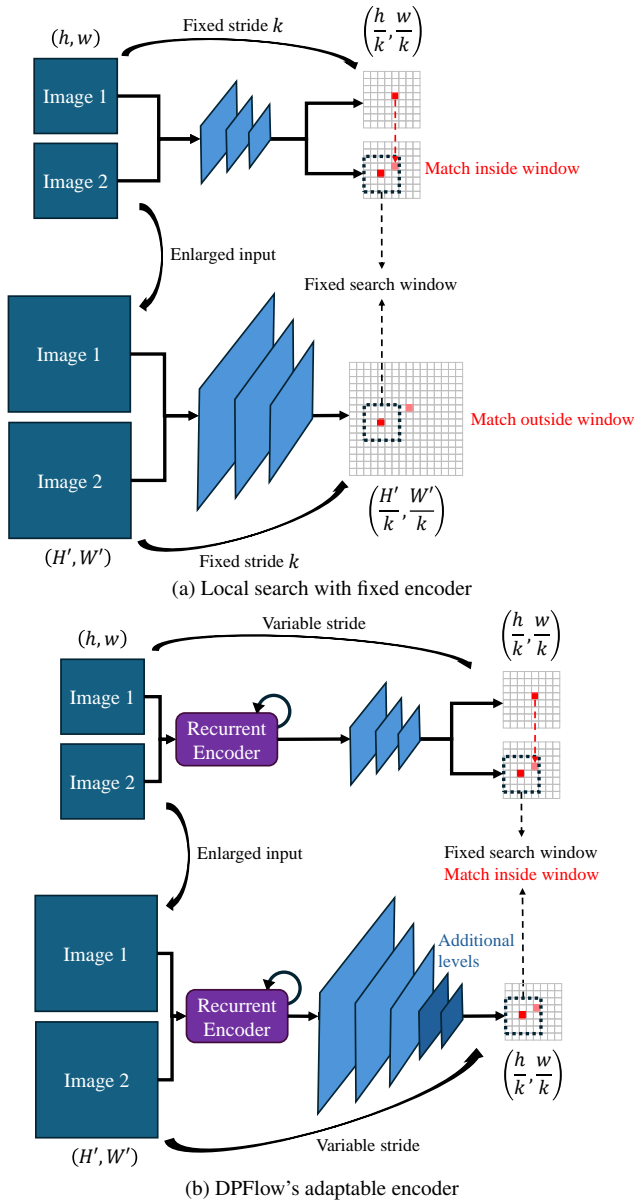


Figure 12. Simple example of the local matching procedure on typical optical flow models. (a) The spatial size of the feature map extracted by an encoder with a fixed structure is determined by the encoder's total stride k (e.g., 8 times smaller than the input). When the input resolution increases, the matched points are beyond the local window's range, causing a mismatch. (b) DPFlow adopts a recurrent encoder that can be dynamically unfolded to change the number of encoding levels and control the size of the initial feature map. This alleviates the window range problem.

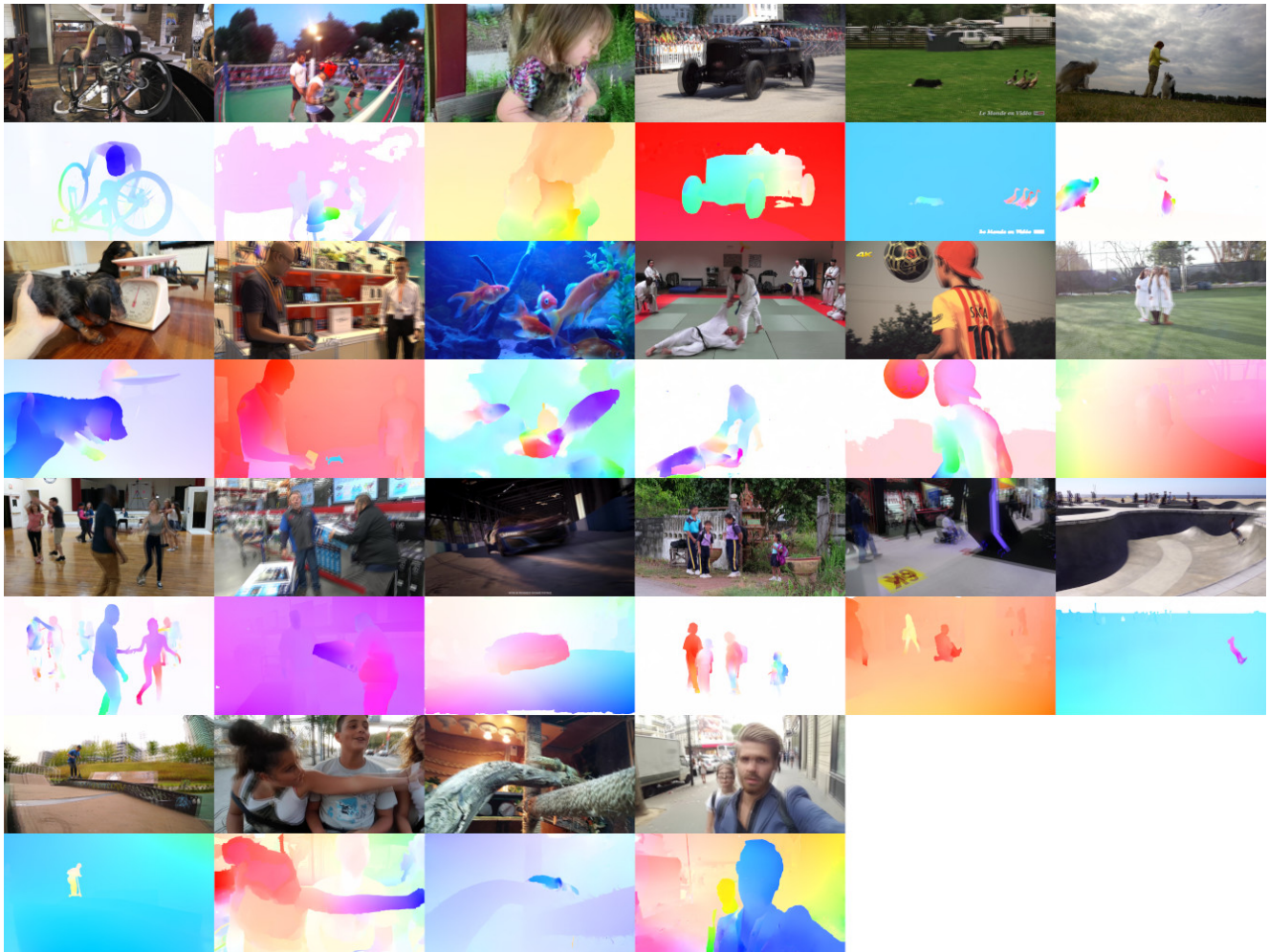


Figure 13. Qualitative results on 4K samples from the DAVIS dataset [40].



Figure 14. Qualitative results on 3K samples from the Middlebury-ST dataset [44].

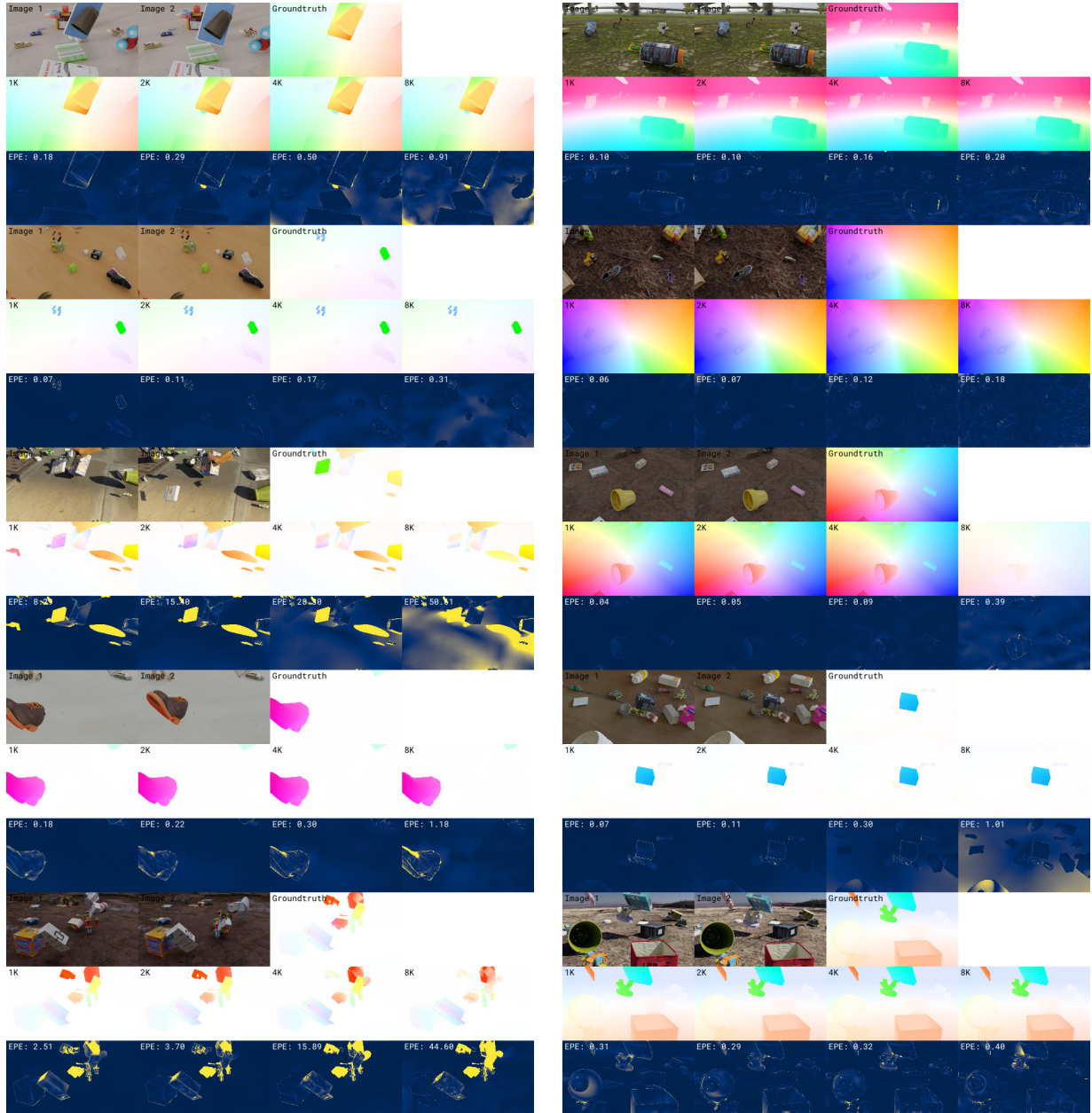


Figure 15. Qualitative results on 1K to 8K samples from our Kubric-NK dataset.

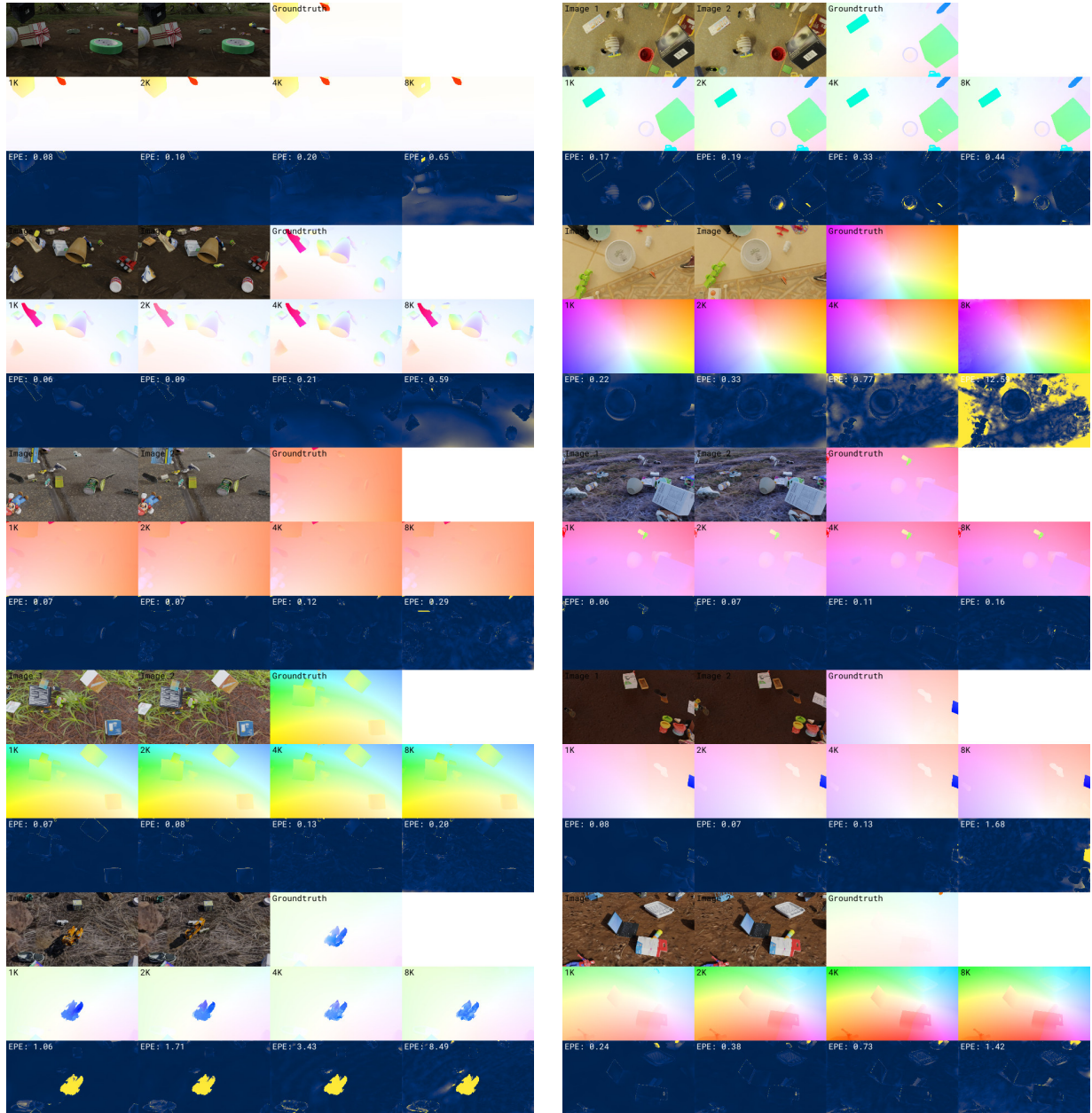


Figure 16. Qualitative results on 1K to 8K samples from our Kubric-NK dataset.

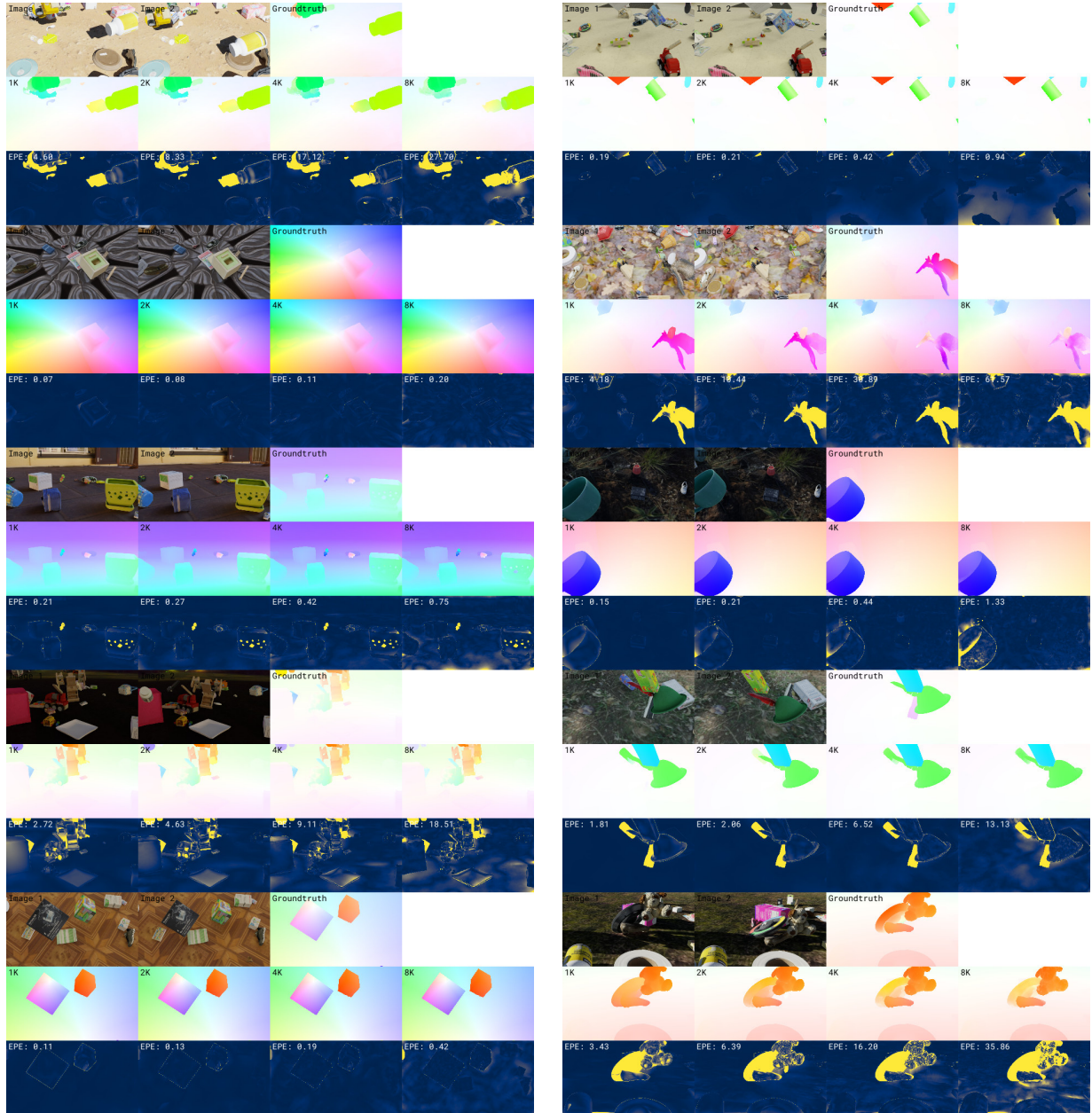


Figure 17. Qualitative results on 1K to 8K samples from our Kubric-NK dataset.